Article

Charge Transfer Kinetics and Thermodynamics Control the Energy Conversion Efficiency of a Gallium Phosphide Solar Hydrogen Photocathode

Kathleen Becker, Li Wang, and Frank E. Osterloh*

Read Online

| ACCESS | Metrics & More | Article Recommendations | SI Supporting Information |

ABSTRACT: P-type gallium phosphide (GaP) photocathodes for hydrogen evolution from water have a theoretical energy conversion efficiency of 12% based on the 2.4 eV optical band gap of the material. The performance of actual GaP photocathodes is much lower, for reasons not entirely clear. Here we use vibrating Kelvin probe surface photovoltage (VKP-SPV), open circuit potential (OCP) measurements, and photoelectrochemical (PEC) experiments to evaluate the kinetic and thermodynamic factors that control energy conversion with GaP photocathodes for the hydrogen evolution reaction (HER). We find that the open circuit photovoltage of the bare GaP-H$_2$O junction is limited by

recombination at surface states and that an CdS overlayer increases both photovoltage and photocurrent due to formation of a n-p-junction. An optimized GaP/CdS/Pt photocathode drives hydrogen evolution with a quantum efficiency of 62% at 400 nm and 0.0 V RHE and an open circuit photovoltage of 0.43 V at 250 mW cm^{-2}. The Pt cocatalyst increases the photocurrent due to improve HER kinetics but reduces the photovoltage by promoting recombination. Added hydrogen or oxygen gas raise or lower the photovoltage by modifying the electrostatic barrier (band bending) in GaP. This shows that the GaP/CdS junction is not "buried" but behaves like a Schottky junction whose charge separating properties are controlled by the electrochemical potential of the electrolyte. The dynamic junction properties need to be considered in the design of optimized hydrogen evolution photoelectrodes and photocatalysts. Additionally, the work reveals that PEC or OCP measurements tend to underestimate the photovoltage because they do not account for changes in the electrochemical potential at the electrode-liquid contact. In contrast, the VKP-SPV method provides the open circuit photovoltage value directly. By combining the photovoltage data with OCP data, the minority carrier electrochemical potential at the electrode-liquid contact can be measured in a contactless way. This provides an improved understanding of illuminated photoelectrodes for the production of solar fuels.
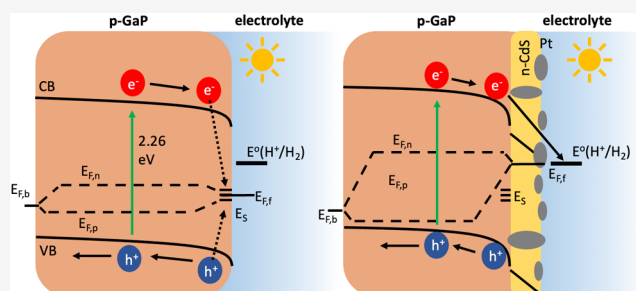
INTRODUCTION

The solar water splitting reaction is a potential avenue to carbon free fuels.[1−3] Buried junction or photovoltaic/electrolyzer devices,[4,5] where photovoltage generation and water redox reactions occur in different parts of the device, generally produce the highest performances. Semiconductor-liquid junctions have lower efficiency[6,7] because the junctions have to perform charge separation and multistep redox reactions simultaneously. Because water oxidation and reduction are kinetically slow, they lead to trapped charges at electrode surface, that not only degrade the junctions but also often corrode the semiconductors.[8] Only very few semiconductors are stable and efficient under the corrosive conditions of the water splitting process.[9] This includes the 9.2% efficient InGaN/GaN nanowire array which is protected by a corrosion-resistant N enriched surface layer.[10] Also, BiVO$_4$:Mo photoanodes for water oxidation also have shown long-term operation[11] and high efficiency in combination with WO$_3$.[12,13] High stability is seen

also for Al-doped SrTiO$_3$, although this comes at the expense of low conversion efficiency resulting from the large band gap.[14,15]

Gallium phosphide (GaP) is a III−V semiconductor with a zincblende crystal structure and a conduction band edge approximately −1.2 V relative to the proton reduction potential.[8,16] Based on its 2.26 eV bandgap,[16] GaP has a theoretical maximum solar to hydrogen (STH) efficiency of 12%. We recently demonstrated that n-GaP photocatalyst particles can generate H$_2$ from aqueous electrolytes with up to 14.8% quantum efficiency (525 nm).[17] While some nano-structured GaP photoelectrodes achieve a STH of up to 2.9% for hydrogen evolution,[18] most other GaP photocathodes support
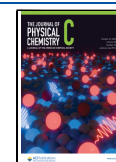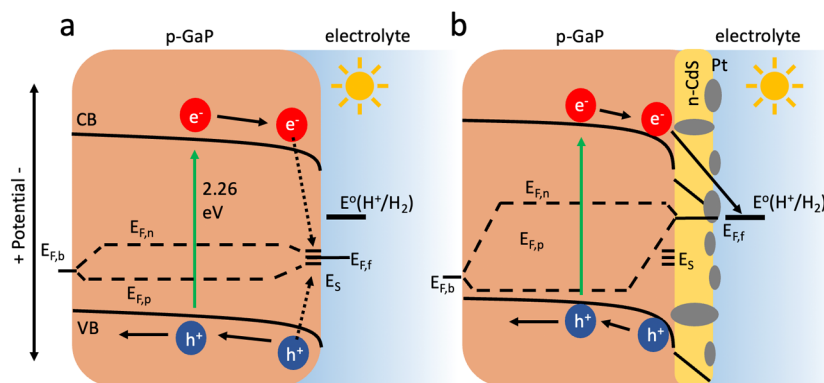
Figure 1. Energetics and charge transfer at illuminated photocathode−electrolyte contacts. (a) Bare GaP electrode and (b) GaP/CdS/Pt electrode. The photovoltage V_{Ph} is the difference between the electrochemical potentials $E_{F,f}$ and $E_{F,b}$ at the front and back, respectively. Quasi Fermi levels are shown also. The photovoltage of the bare electrode is limited by recombination at surface states of energy E_S (dotted arrows). Direct electric contact between Pt particles and the GaP wafer allows the electrolyte properties to control the junction.

only modest hydrogen evolution rates.[19−21] GaP photoelectrodes also suffer from significant corrosion in aqueous solutions[18] requiring metal oxide passivation layers,[21−24] or covalent surface modifications for protection.[25]

Here we show for the first time that the performance and stability of GaP photocathodes can be improved by chemical bath deposition of CdS overlayers followed by photodeposition of Pt cocatalysts. A detailed spectroscopic and photoelectrochemical (PEC) analysis reveals that photocurrent and photovoltage of the resulting devices are not only affected by the CdS layer and the cocatalyst, but also depend sensitively on the pH of the electrolyte and the presence of hydrogen and oxygen gases. This characterizes the GaP/CdS/Pt photoelectrode as Schottky junction,[3,17,26−30] whose rectifying property is controlled by the electrochemical potential of the electrolyte. Optimized performance requires a balance between the thermodynamics of charge transfer (controls the photovoltage) and its kinetics (controls the photocurrent), as shown in the following.

RESULTS AND DISCUSSION

GaP electrodes were fabricated by cutting a commercial Zn doped GaP wafer (carrier density of 6.8×10^{17} cm^{-3}) into 1×2 cm^2 pieces and by etching them for 10 min with Piranha acid. Electric contact was established with a Cu metal clip to both sides of the wafer. All measurements were performed on the rough side of the wafer after masking the polished side with polyester tape. In assessing the performance of the electrode, we focus on the open circuit photovoltage V_{Ph} as the principal measure of the maximum possible electric energy output. V_{Ph} is given by the difference between the Fermi levels at the front and back of the illuminated photoelectrode (Figure 1 and eq 1) at zero current.[31,32]

$$V_{Ph} = E_{F,front} - E_{F,back} \tag{1}$$

The open circuit photovoltage can be obtained from experimental data in several ways. For example, according to eq 2, a PEC scan of the illuminated electrode yields the open circuit photovoltage from the difference of the photocurrent onset potential $E_{On}(light)$ and the electrochemical potential $E^0(Ox/red)$ of the corresponding redox couple. This method is widely used[33,34] but its disadvantage is that E^0 is not always known, e.g., when the identity of the redox couple is not clear, in the presence of multiple charge transfer processes,[30] or when

additional redox states from cocatalysts,[35] photocorrosion, or Fermi level pinning[36] are present.

$$V_{Ph}(PEC) = E_{On}(light) - E^0(Ox/red) \tag{2}$$

$$V_{Ph}(OCP) = OCP(light) - OCP(dark) \tag{3}$$

$$V_{Ph}(SPV) = SPV = CPD(light) - CPD(dark) \tag{4}$$

Equation 3 provides the open circuit photovoltage as the difference of the open circuit potentials in the dark and under illumination. This method is commonly used in the literature,[30,37−39] but its shortcoming is that it assumes that the electrochemical potential at the electrode front, $E_{F,f}$ remains constant when turning on the light. This is often the case for fast redox couples, but not for slow ones, which have a large kinetic overpotential. As we showed recently, a third, and more direct way to obtain the open circuit photovoltage is vibrating Kelvin probe surface photovoltage (VKP-SPV) spectroscopy.[31,32,40] This method employs a vibrating gold Kelvin probe to measure the contact potential difference (CPD) of the photoelectrode relative to gold. A SPV signal is obtained from the light-induced change of the CPD (eq 4). For conductive semiconductors that are in electrochemical equilibrium with their adjacent phases, the SPV equals the open circuit photovoltage $V_{Ph}(SPV)$. As will be demonstrated in the following, $V_{Ph}(SPV)$ is the most reliable assessment of V_{Ph}. In combination with eq 1 it provides the absolute electrochemical potential $E_{F,f}$ at the front of the GaP photoelectrode as a function of the light intensity. Values for $E_{F,f}$ are not accessible through standard OCP and PEC measurements, but can be obtained with specialized techniques that use added electrodes or atomic force microscopy probes.[33,41]

The PEC properties of the etched GaP wafer in 0.1 M H$_2$SO$_4$ (pH of 0.9) under N$_2$ atmosphere are shown in Figure 2 and Table 1. Under simulated 1 sun illumination, the GaP wafer produces a cathodic photocurrent of −0.16 mA/cm^2 at 0 V vs RHE with a photocurrent onset of 0.30 V vs RHE. LED illumination at 400 nm produces a photocurrent of −0.36 mA/cm^2 corresponding to a photon-to-current-conversion efficiency (IPCE) of 2.53%. Repeat scans (Figure S1a) show a ~50% decrease in photocurrent and a cathodic shift of the onset potential, indicating electrode degradation during PEC. This is not surprising considering the positive value of the cathodic corrosion potential of GaP (0.25 V RHE).[8] This competing corrosion reaction makes it impossible to determine the nature
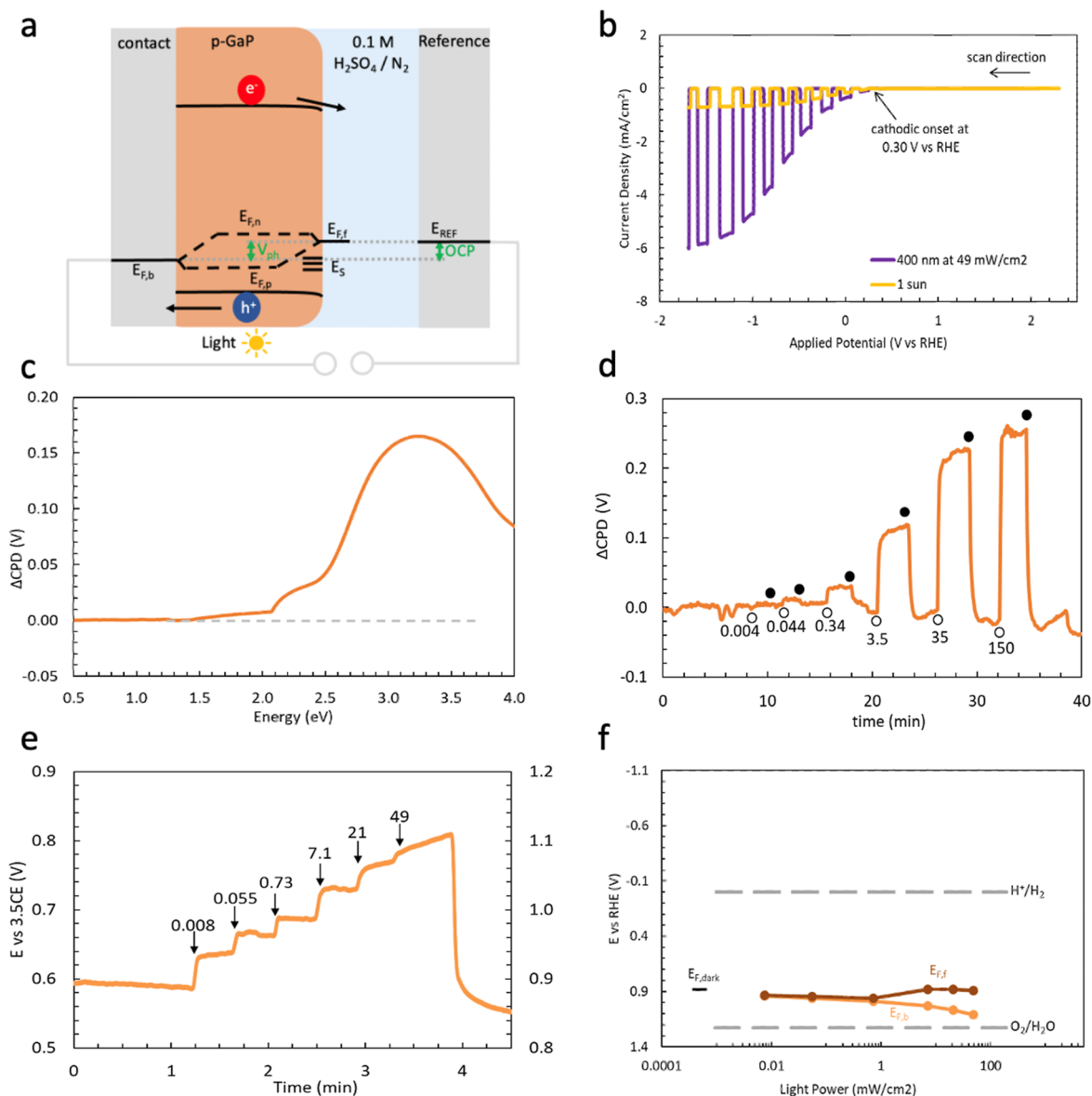
Figure 2. GaP electrode in aqueous H_2SO_4 at pH 0.9 under N_2 flow. (a) Qualitative scheme of the illuminated junction. (b) Linear sweep voltammetry scans under chopped 1 sun or 400 nm (49 mW/cm²) illumination. Repeat scans are shown in Figure S1a. (c) SPV spectrum under Xe lamp illumination (0.1−1.0 mW/cm²) in 0.1 M H_2SO_4 and N_2 flow. The discontinuities at 1.28 and 2.07 eV are from optical filter changes. (d) SPV under intermittent illumination from 405 nm LED (irradiance in mW/cm²). (e) OCP under intermittent illumination from 400 nm LED (irradiance in mW/cm²). (f) Fermi level diagram with $E_{F,b}$ from OCP data and $E_{F,f}$ from SPV data and eq 1. Emission profiles of the Xe arc lamp and of the LEDs are shown in Figure S2.

Table 1. Electrode Properties from LSV, SPV, and OCP Measurements

| sample	V_{Ph}(PEC) 1 sun (V vs RHE)	j_{ph} 400 nm 0 V vs RHE (mA/cm²)	IPCE at 400 nm (%)	V_{Ph}(SPV) under max (113−250 mW cm²) 405 nm illumination (V)	R (s⁻¹ cm⁻²)	V_{Bi} from dark OCP	V_{Ph}(OCP) under max (49−100 mW cm²) 400 nm illumination (V)
etched pGaP	0.30	−0.36	2.53	0.27	$<9.0 \times 10^{13}$	0.47	0.23
GaP/Pt	0.55	−3.78	24.0	0.38	$<9.0 \times 10^{13}$	1.09	0.31
GaP/CdS	0.76	−1.61	10.1	0.64	$<8.2 \times 10^{12}$	1.09	0.27
GaP/CdS/Pt	0.59	−9.66	62.0	0.43	$<1.6 \times 10^{13}$	1.07	0.26
Na_2SO_4/100% N_2	0.56	−1.7	10.8	0.17	$<9.2 \times 10^{12}$	0.40	0.13
Na_2SO_4/100% O_2	0.62	−0.26	1.64	0.12	$<9.0 \times 10^{13}$	0.35	0.18
Na_2SO_4/10% H_2, 90% N_2	0.31	−0.41	1.96	0.44	$\ll 1.0 \times 10^{13}$	1.04	0.30
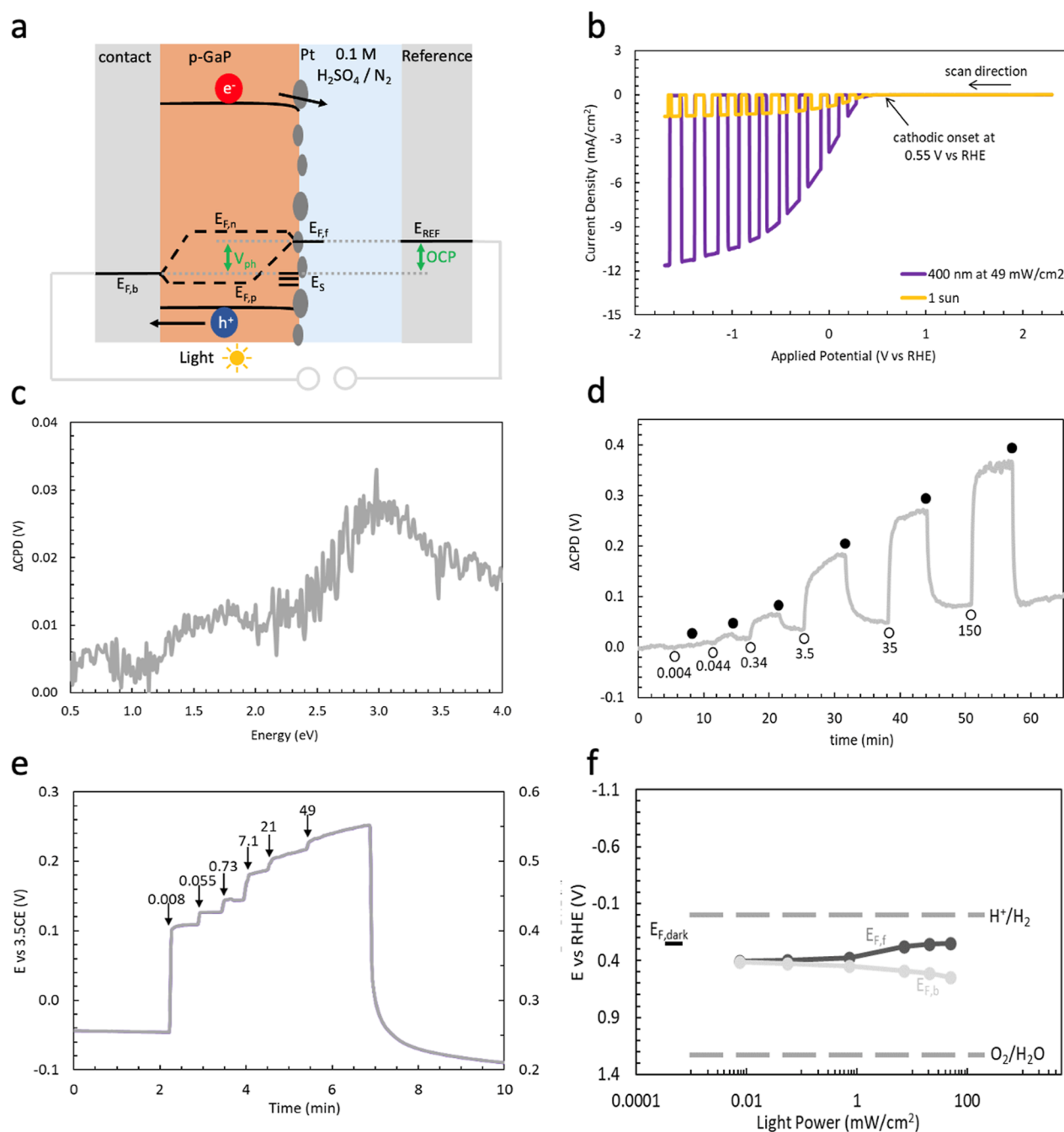
Figure 3. GaP/Pt in aqueous H_2SO_4 at pH 1.0 under N_2 flow. (a) Qualitative junction scheme under illumination. (b) Linear sweep voltammetry scans under chopped illumination. (c) SPV spectrum. (d) Intensity dependent SPV from a 405 nm LED displayed in mW/cm². (e) Intensity dependent OCP under 400 nm LED illumination (mW/cm²) versus calomel electrode (left) and RHE (right). (f) Fermi level diagram with $E_{F,b}$ from OCP data and $E_{F,f}$ from SPV data and eq 1.

of the Faraday process or the photovoltage from the PEC scan in Figure 2b.

Hydrogen evolution is not obvious as there is no detectable gas evolution at the electrode. In order to independently measure the photovoltage, SPV spectra were recorded for GaP immersed in a 0.1 M H_2SO_4 (wet N_2 atmosphere), using the liquid SPV configuration described previously (Figure S3).[31,32,40] According to Figure 2c, a positive photovoltage begins at 2.06 eV, which is near the optical band gap (2.18 eV) of the wafer (see diffuse reflectance spectrum in Figure S4). The largest SPV signal of 0.16 V occurs at 3.28 eV, where GaP absorbs strongly and the intensity from the Xe emission has a

secondary maximum. The photovoltage spectrum is similar to earlier observations[42] and can be attributed to charge separation under GaP band gap excitation, as shown in Figure 2a. Here the photoelectrons move toward the GaP surface, where the Kelvin probe is located, and photoholes move to the back of the wafer. The spectrum in Figure 2c also shows a weak SPV signal at 1.5–2.0 eV, which is attributed to the excitation of GaP mid gap states. Our previous study on n-GaP shows that such states are due to oxide and Ga(3+) on the GaP surface.[17]

During the SPV scan, $V_{Ph}(SPV)$ is limited by the low light intensity from the monochromator $(1-2\ mW\ cm^{-2})$. To obtain $V_{Ph}(SPV)$ as a function of the irradiance, SPV data was recorded
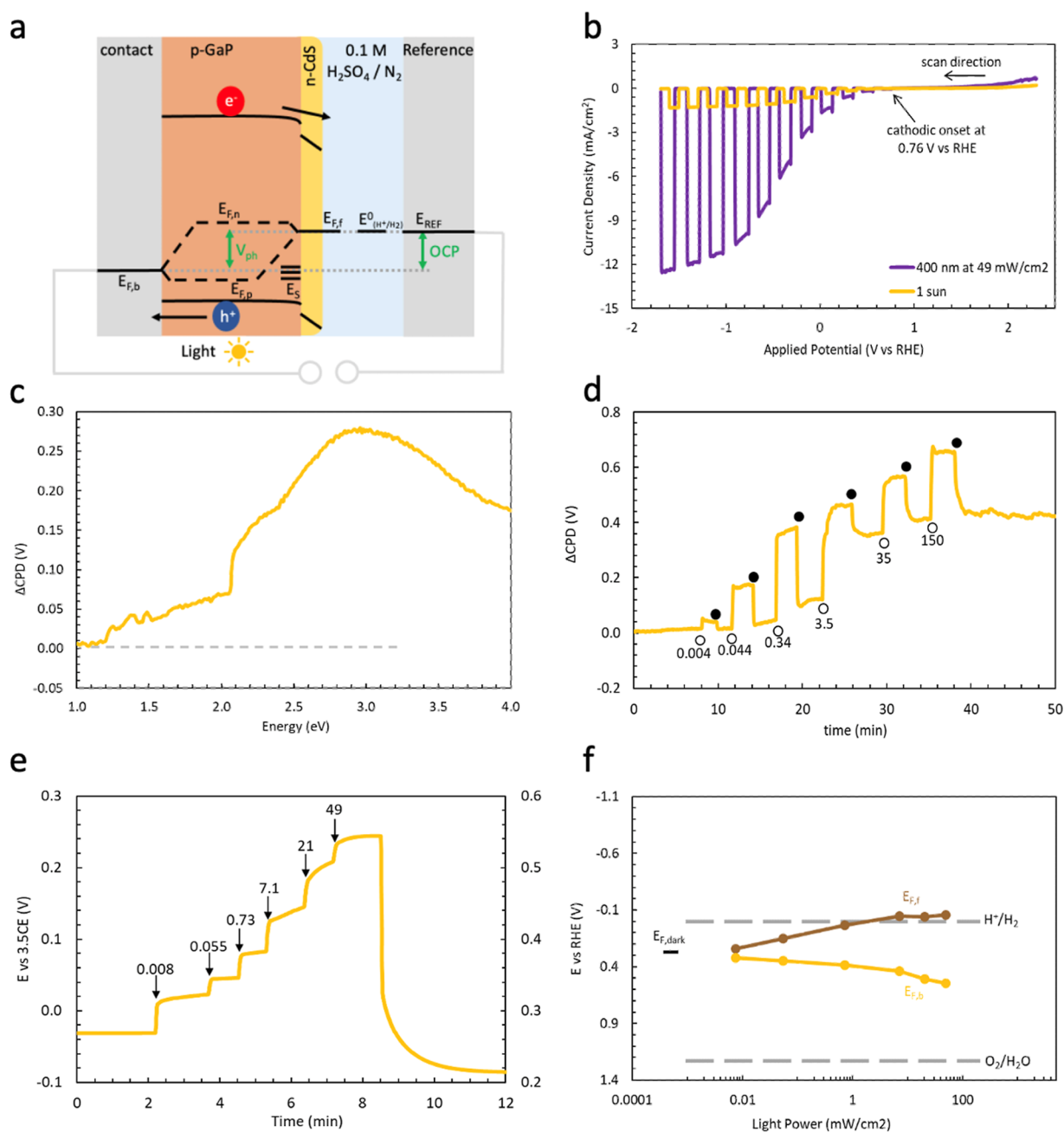
Figure 4. GaP/CdS electrode in aqueous H_2SO_4 at pH 0.8 under N_2 flow. (a) Qualitative junction scheme under illumination. (b) Linear sweep voltammetry scans under chopped illumination from a 400 nm LED (49 mW cm^{-2}) and simulated sunlight. (c) SPV spectra. (d) Intensity dependent SPV from a 405 nm LED displayed in mW/cm^2. (e) Intensity dependent OCP under 400 nm LED illumination (mW/cm^2), versus calomel electrode (left) and RHE (right) (f) Fermi level diagram with $E_{F,b}$ from OCP data and $E_{F,f}$ from SPV data and eq 1.

with intermittent illumination from a 405 nm LED. Figure 2d shows that reversible SPV signals form and decay on the 10 s times scale. This is fast in comparison to metal oxide films, where SPV generation and decay can occur on the 600 s time scale.[43,44] The fast dynamics are attributed to the higher mobility of charge carriers in GaP.[16] The SPV signals show a linear dependence on the logarithmic light intensity (Figure S5a) as expected from the diode equation for an ideal junction. Under 150 mW cm^{-2} the photovoltage reaches 0.26 V. This equals ~10% of the band gap of the material, suggesting severe electron hole recombination, possibly at GaP surface states. The recombination rate can be estimated from the lowest irradiance needed to produce a SPV signal (0.044 mW/cm^2 in Figure 2d). Below this threshold

intensity, charges recombine as quickly as they are generated. Based on the photon flux Φ_q from the LED, the charge carrier recombination rate R is slighly less than $R < \Phi_q = 9.0 \times 10^{13}$ s^{-1} cm^{-2}.

Next, the electrochemical potential $E_{F,b}$ at the backside of the GaP electrode was obtained from the OCP of the working electrode versus the reference electrode (Figure 2e). In the dark, $E_{F,b} = 0.88$ V vs RHE appears to be mainly controlled by the E_F of GaP (Figure S6). Under illumination, $E_{F,b}$ moves to more oxidizing values, in support of the charge separation direction shown in Figure 2a. Based on the potential variation $E_{F,b}$ (light) − $E_{F,b}$ (dark), the OCP photovoltage V_{Ph}(OCP) can be estimated as 0.23 V at 49 mW cm^{-2}. This agrees well with

V_{Ph}(SPV) = 0.22 V at 35 mW cm^{-2}. Using eq 1, the Fermi level $E_{F,f}$ at the GaP front can now be calculated for each irradiation condition. The data is plotted in Figure 2f versus the logarithmic irradiance. Under illumination, $E_{F,b}$ moves to oxidizing potentials with increasing light intensity, whereas $E_{F,f}$ remains near the dark Fermi level, and much below the proton reduction potential. This confirms that the reducing ability of the photocathode is limited, and that no electron transfer to the solution can take place due to the lack of suitable electron acceptors. Photogenerated electrons either recombine or become trapped in surface states. Overall, the data in Figure 2 illustrates a severely degraded photocathode function for the p-GaP/H$_2$O(N$_2$) interface.

Next, to evaluate the effect of a Pt cocatalyst on the performance of the photocathode, Pt nanoparticles were grown on the GaP wafer by photoelectrodeposition (Figure S7). According to scanning electron microscopy (SEM), the particles are <50 nm in size and irregularly distributed on the rough GaP surface (Figure S8). The PEC properties of the GaP/Pt electrode in 0.1 M H$_2$SO$_4$ under N$_2$ atmosphere are summarized in Figure 3. The addition of Pt moves the onset potential in anodic direction, corresponding to an improved photovoltage of V_{Ph}(PEC) = 0.55 V (Figure 3b). The photocurrent reaches 3.8 mA/cm^2 at 0 V vs RHE resulting in a much-improved incident photon to current efficiency of 24.0% under 400 nm illumination. At low light intensity, the photovoltage in Figure 3d is very small, indicating increased electron−hole recombination at the GaP/Pt contact. Based on the nonzero SPV signal at 0.044 mW cm^{-2} the electron−hole recombination rate is estimated as 9.0×10^{13} s^{-1} cm^{-2}, similar to the bare GaP contact above. The actual value may be higher, considering the noisy photovoltage spectrum in Figure 3c. That spectrum also reveals sub-bandgap states in the 1.2−2.0 eV range, and an effective bandgap at 2.06 eV, similar to Figure 2c. Again, the SPV signal increases with illumination intensity (Figure 3d). A small positive drift of the CPD baseline is attributed to electron trapping at the GaP/Pt surface.

OCP measurements in Figure 3e place the GaP/Pt/H$_2$SO$_4$(N$_2$) resting potential at 0.25 V vs RHE, down from 0.88 V RHE for the bare GaP surface. This cathodic shift of the Fermi level is likely due to partial reduction of the GaP surface during the cathodic photodeposition of Pt. Under illumination, a photovoltage of 0.31 V is generated at 49 mW cm^{-2}, based on the variation of the OCP. This is a minor improvement over the bare GaP photoelectrode (0.22 V at 35 mW cm^{-2}). The Fermi level diagram in Figure 3f describes the photovoltage of the GaP/Pt/H$_2$SO$_4$(N$_2$) photoelectrode at open circuit. Both Fermi levels change with increasing illumination intensity, but no electron transfer to the electrolyte can occur because $E_{F,f}$ never reaches the E^0 for the proton reduction. The photovoltage trend is similar to that of the bare GaP electrode, except that both $E_{F,n}$ and $E_{F,f}$ are more about 0.5 V more reducing. This is attributed to the possible reduction of the GaP surface during the cathodic photodeposition of the Pt cocatalyst, which populates some of the surface Ga(3+) states with electrons. Overall, the data shows that the addition of the Pt cocatalyst does *not* improve the open circuit photovoltage of the electrode. However, it does significantly increase the photocurrent at 0 V RHE applied potential (Figure 3b), by speeding up electron transfer to the H$^+$/H$_2$ couple.

According to the literature, TiO$_2$, ZnS, and CdS buffer layers have the ability to passivate surface states resulting from corrosion states and dangling bonds.[29,32−34,45] For this study we chose CdS because of the favorable band alignment in Figure S6. The CdS layer was grown by chemical bath deposition from cadmium(II) acetate dihydrate and thiourea at basic pH. Based on SEM and energy dispersive X-ray (EDX) in Figures S9 and S10, the CdS film is conformal and ∼380 nm thick. PEC data for a GaP/CdS electrode in aqueous H$_2$SO$_4$ at pH 0.8 under N$_2$ flow is shown in Figure 4b. The PEC scan reveals a greatly improved performance over the bare GaP electrode. The photocurrent is −1.6 mA/cm^2 at 0 V vs RHE, corresponding to an incident photon to current efficiency of 10.1%. The photovoltage V_{Ph}(PEC) = 0.76 V (based on the 0.76 V RHE photocurrent onset potential) is improved over the previous 0.3 V value. Hydrogen is evolved visibly as gas bubbles at the working electrode, although after 3 repeat scans, the bubbles cause the CdS layer to peel off the GaP wafer. The CdS layer also increases both the band gap SPV (0.28 V at 3.03 eV) (Figure 4c) and the sub-band gap signal at 1.2−2.1 eV. Strong sub-band gap signals often result when charge carriers in midband gap states are polarized by strong electric fields.[46] This further demonstrates how the CdS increases the band bending in GaP. The intensity dependent SPV in Figure 4d reaches 0.68 V at 150 mW cm^{-2}, almost three times the previous value. Unlike bare GaP, GaP/CdS produces an SPV signal even under the smallest tested light intensity (4 μW cm^{-2}). This means the recombination rate is less than the photon flux at this intensity (8.2×10^{12} s^{-1} cm^{-2}). Also, a plot of the SPV signal versus the logarithmic light intensity is linear for the entire intensity range (Figure S5b), suggesting near ideal behavior of the photodiode. However, a very significant drift of the SPV baseline in Figure 4d to more positive values suggests that electrons are trapped in the CdS surface or at states at the GaP/CdS interface.

According to OCP data in Figure 4e, the $E_{F,b}$ of the GaP/CdS electrode is 0.27 V vs RHE in the dark, compared to 0.88 V vs RHE for the bare GaP. This proves that the CdS layer controls the Fermi level in the GaP electrode with its reducing work function and that a p-n-junction forms at the GaP/CdS interface. Based on the $E_{F,b}$ variation under illumination, the GaP/CdS/H$_2$SO$_4$(N$_2$) electrode produces a photovoltage of V_{Ph}(OCP) = 0.27 V at 49 mW cm^{-2}, slightly higher than what seen for the bare GaP wafer (0.23 V at 49 mW cm^{-2}). This increase agrees with the improved photovoltage seen in the SPV experiments. Please note that V_{Ph}(OCP) values fall behind V_{Ph}(SPV) values over the entire illumination range (Figure 4d,e). This discrepancy is due to the shortcomings of the OCP measurement, which probes the change in the back potential ($E_{F,b}$) while ignoring any drift of the front potential ($E_{F,f}$) to more reducing values. This becomes obvious in the Fermi level plot in Figure 4f, which shows considerable variation of *both* Fermi levels with light intensity. The drift in $E_{F,f}$ is attributed to electron trapping in the CdS layer, as mentioned above. Eventually, at 0.725 mW cm^{-2}, $E_{F,f}$ at the GaP/CdS front reaches the proton reduction potential, allowing the hydrogen evolution reaction (HER) to proceed without applied external bias. This agrees with the observation of gas evolution at the working electrode. As a result of the charge transfer equilibrium, $E_{F,f}$ becomes pinned at E^0(H$^+$/H$_2$). Meanwhile, the hole Fermi level moves to more oxidizing potentials with light intensity, as expected from the Diode equation. Overall, these data demonstrate that introduction of a p-n-junction at the GaP/CdS interface in Figure 4a improves the solar energy conversion efficiency. However, the photocurrent at 0 V RHE remains lower than for the GaP/Pt system, due to a large kinetic proton reduction overpotential at CdS.[47]
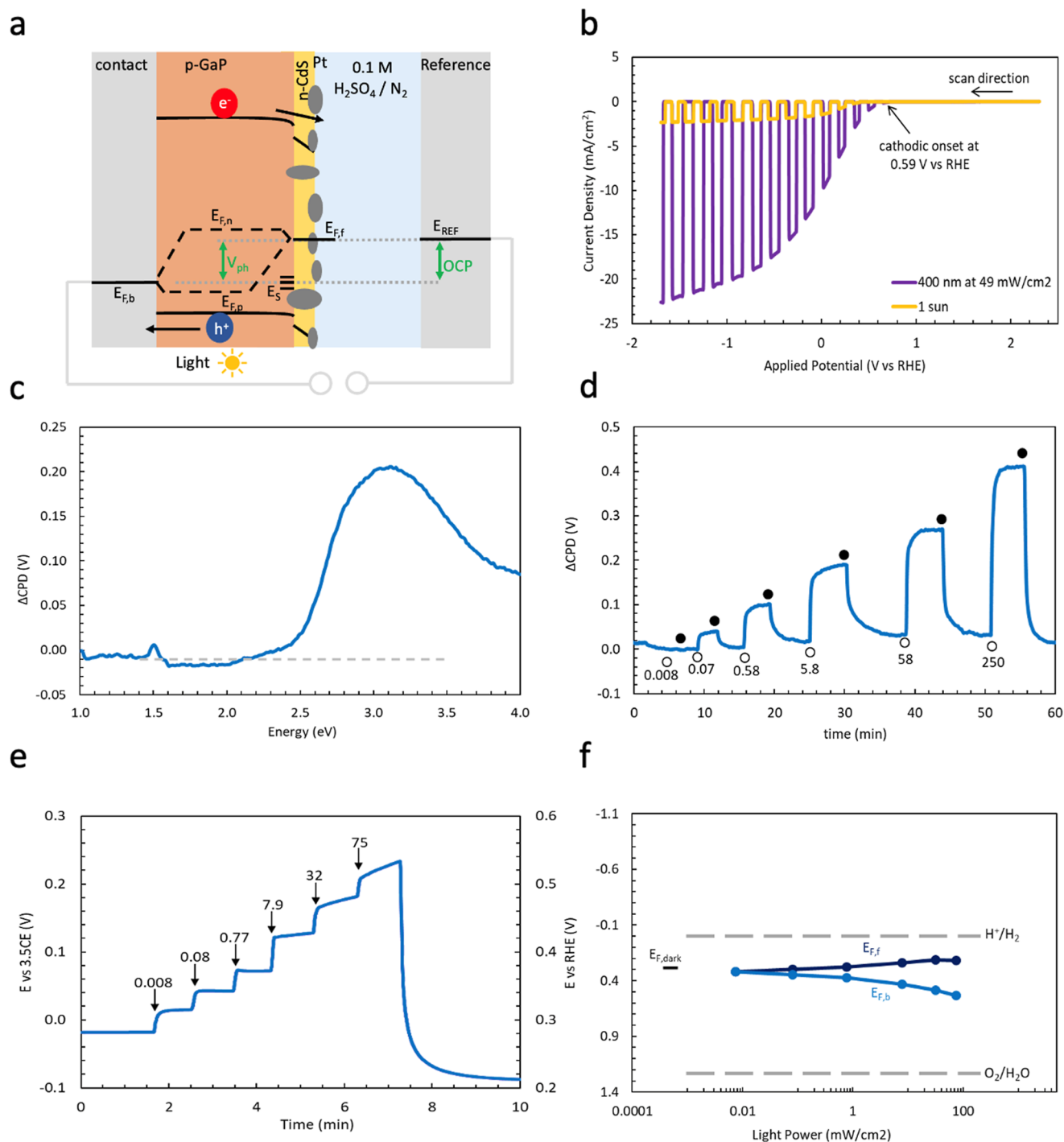
Figure 5. GaP/CdS/Pt in aqueous H_2SO_4 at pH 0.9 under N_2 flow. (a) Qualitative junction scheme under illumination. (b) Linear sweep voltammetry scans under chopped illumination. (c) SPV spectrum under Xe lamp illumination. (d) Intensity dependent SPV from a 405 nm LED with irradiance displayed in mW/cm². (e) Intensity dependent OCP under 400 nm LED illumination (mW/cm²) versus calomel electrode (left) and RHE (right) (f) Fermi level diagram with $E_{F,b}$ from OCP data and $E_{F,f}$ from SPV data and eq 1.

To combine the benefits of the p-n-junction and the reduced proton reduction overpotential of Pt, a GaP/CdS/Pt device was constructed by sequential deposition of CdS and Pt nanoparticles. The PEC properties of the GaP/CdS/Pt electrode are summarized in Figure 5. Under 400 nm illumination (49 mW cm⁻²) a photovoltage V_{ph}(PEC) of 0.59 V and a short circuit photocurrent of 9.8 mA/cm² at 0 V vs RHE are observed resulting in an incident photon to current efficiency of 62% (400

nm). As expected, these values are superior to the previous electrode configurations.

The SPV spectrum of the GaP/CdS/Pt device shows the photovoltage onset shifted to 2.51 eV compared to 2.06 eV for the bare GaP wafer. This is a result of shading by the Pt nanoparticle and CdS layers. Indeed, the optical absorption edge (Figure S4) of the GaP/CdS/Pt stack also shifts to higher energy. The maximum SPV is found at 0.43 V (250 mW cm⁻²), much higher than seen for GaP/Pt, but slightly below the value
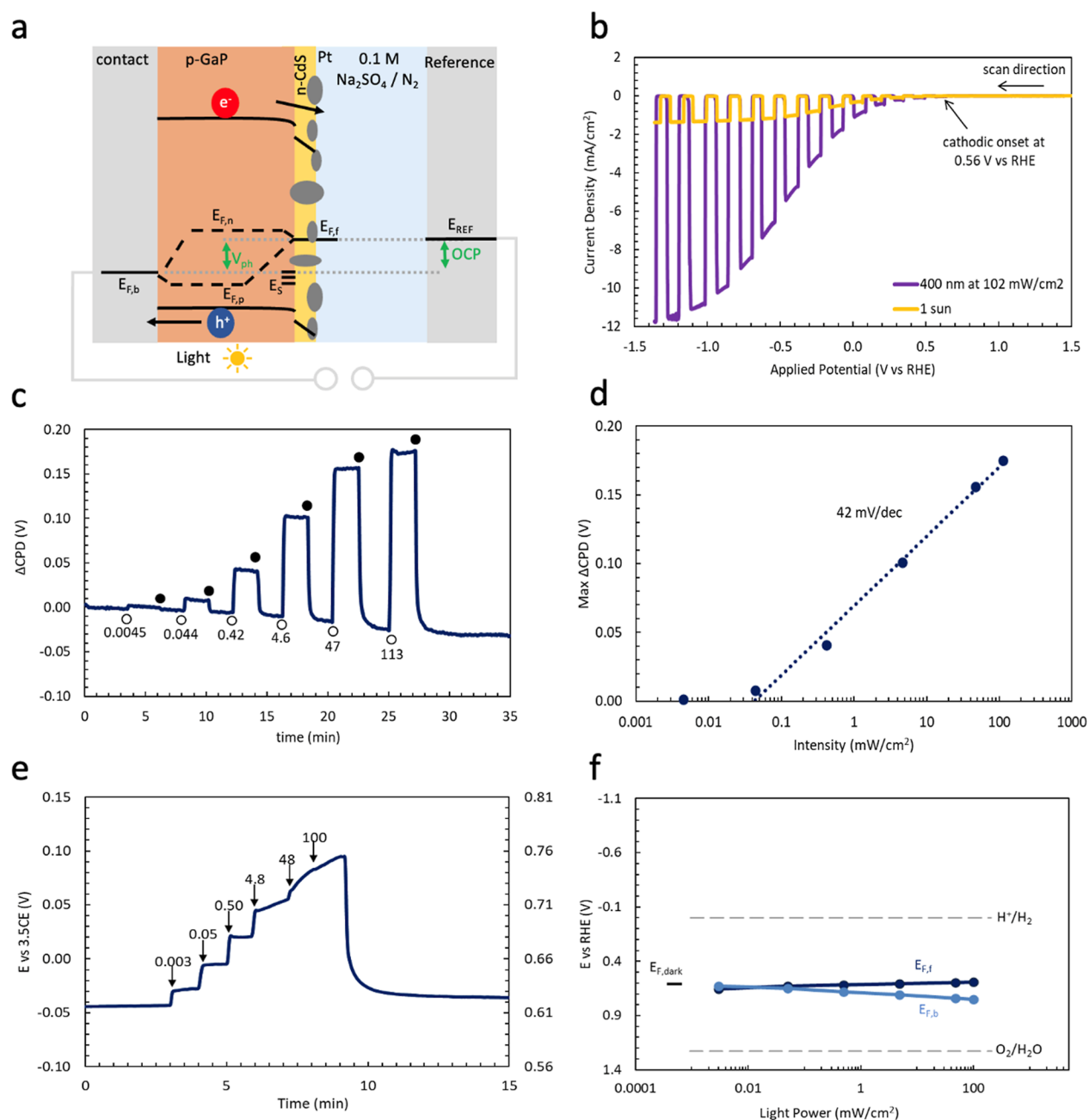
Figure 6. GaP/CdS/Pt in aqueous Na_2SO_4 at pH 6.6 under N_2 flow. (a) Qualitative junction scheme under illumination. (b) Linear sweep voltammetry scans under chopped illumination. (c) Intensity dependent SPV from a 405 nm LED (irradiance given in mW/cm^2) (d) maximum ΔCPD versus logarithm of light intensity. (e) Intensity dependent OCP under 400 nm LED illumination (mW/cm^2) versus calomel electrode (left) and RHE (right) (f) Fermi level diagram with $E_{F,b}$ from OCP data and $E_{F,f}$ from SPV data and eq 1.

observed for the GaP/CdS sample. Additionally, a SPV is generated only at 0.008 mW cm^{-2} 405 nm LED illumination, indicating that the added Pt increases the electron–hole recombination rate to $R = 1.6 \times 10^{13}$ s^{-1} cm^{-2} relative to the GaP/CdS electrode ($<8.2 \times 10^{12}$ s^{-1} cm^{-2}).

Based on the OCP measurements in Figure 5e, the GaP/CdS/Pt electrode has a similar dark resting potential (0.28 V RHE) as the GaP/CdS electrode, i.e. the Fermi level is again controlled by the reducing CdS work function. The potential shifts to reducing values (0.21 V RHE) after completing an illumination cycle, which is attributed to electron trapping in CdS, as mentioned before. After combining the SPV and OCP data in the Fermi level diagram in Figure 5f, it can be seen that photovoltage

generation by the GaP/CdS/Pt electrode is only 67% of that of the GaP/CdS electrode. Both Fermi levels drift under illumination, but even under the highest illumination intensity of 75 mW cm^{-2} the minority carrier Fermi level $E_{F,f}$ does not quite reach the proton reduction potential. This means HER is not achieved with the unbiased GaP/CdS/Pt electrode in aqueous H_2SO_4/N_2.

The comparison of the data in Figures 4 and 5 shows that the GaP/CdS/Pt junction is not a buried junction with a fixed semiconductor barrier height and photovoltage.[48−52] Instead the electrode behaves like a Schottky type junction whose built in potential depends on the charge transfer kinetics with the electrolyte and the redox potential of the electrocata-
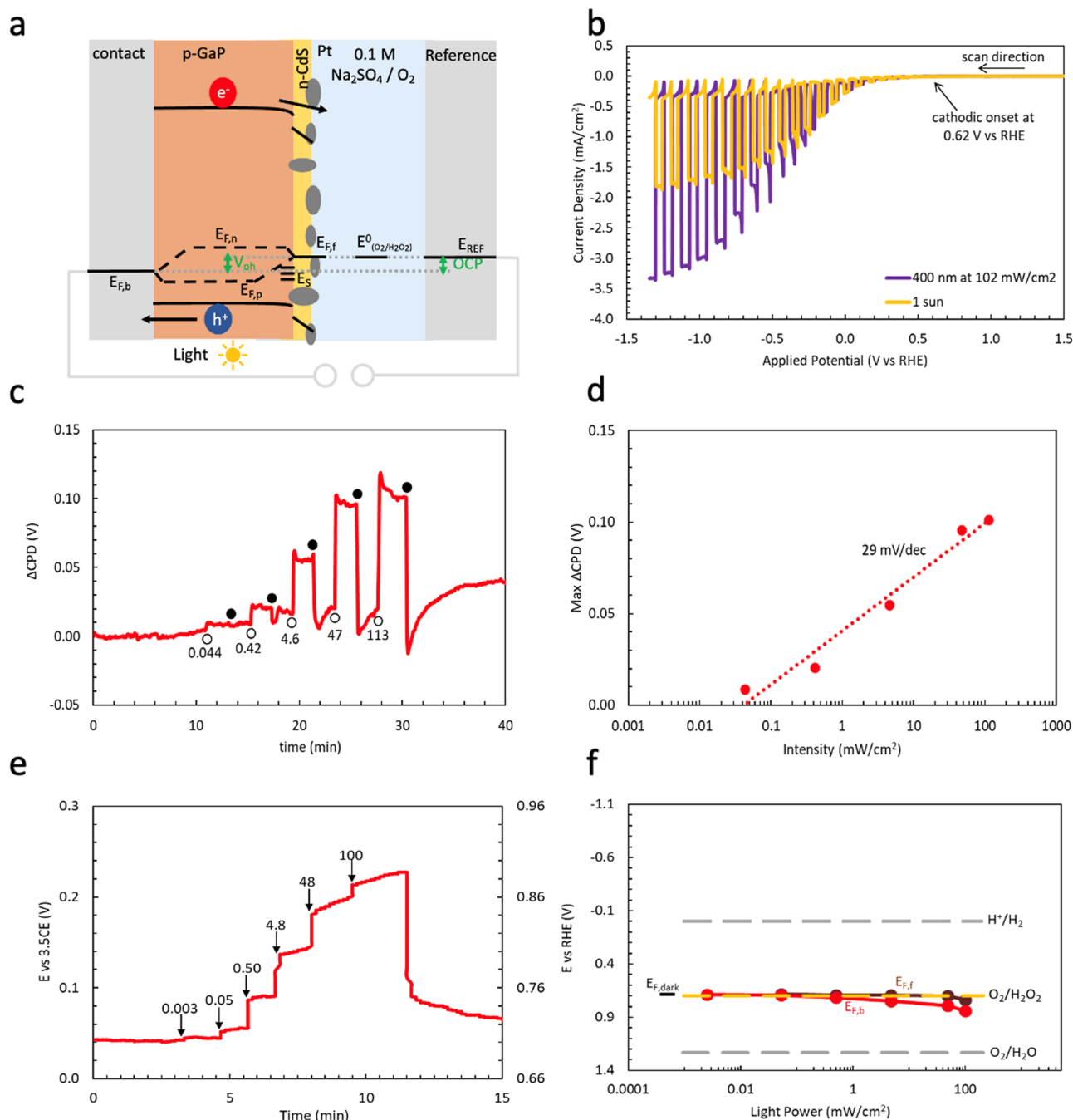
Figure 7. GaP/CdS/Pt in aqueous Na_2SO_4 at pH 6.8 under O_2 flow. (a) Qualitative junction scheme under illumination. (b) Linear sweep voltammetry scans under chopped illumination. (c) Intensity dependent SPV from a 405 nm LED with irradiance values in mW/cm² and (d) maximum ΔCPD versus logarithm of light intensity. (e) Intensity dependent OCP under 400 nm LED illumination (mW/cm²). (f) Fermi level diagram with $E_{F,b}$ from OCP data and $E_{F,f}$ from SPV data and eq 1.

lyst.[3,17,26−30] In N_2-purged H_2SO_4, the built-in potential of the GaP/CdS/Pt junction is ill-defined for lack of a fast redox couple.

To better understand the behavior of the GaP/CdS/Pt electrolyte junction, and its response to the chemical composition of the electrolyte, measurements were repeated in a 0.1 M Na_2SO_4 (pH of 7) in the presence of N_2, H_2 or O_2. Hydrogen and oxygen gases are present during overall water splitting with photoelectrodes and photocatalysts.[30,53,54] Their influence on the energy conversion ability of the GaP photocathodes is therefore of interest. The results in N_2

atmosphere are shown in Figure 6. In this solvent the photovoltage and photocurrent of the electrode are degraded compared to 0.1 M H_2SO_4 (pH of 0.9).

The photocurrent of 1.7 mA/cm² at 0 V vs RHE (IPCE of 10.8%) is only 17% of the value in 0.1 H_2SO_4. This is because the decrease in proton concentration slows down the HER kinetics. While $V_{Ph}(PEC) = 0.56$ V is similar to the electrode in acidic solution (0.59 V), the SPV signal is much smaller (0.18 V under 113 mW cm⁻² compared to 0.25 V under 75 mW cm⁻²). Also, the SPV increases 42 mV per decadic increase in irradiance, while in acidic electrolyte the value is 71 mV dec⁻¹. The
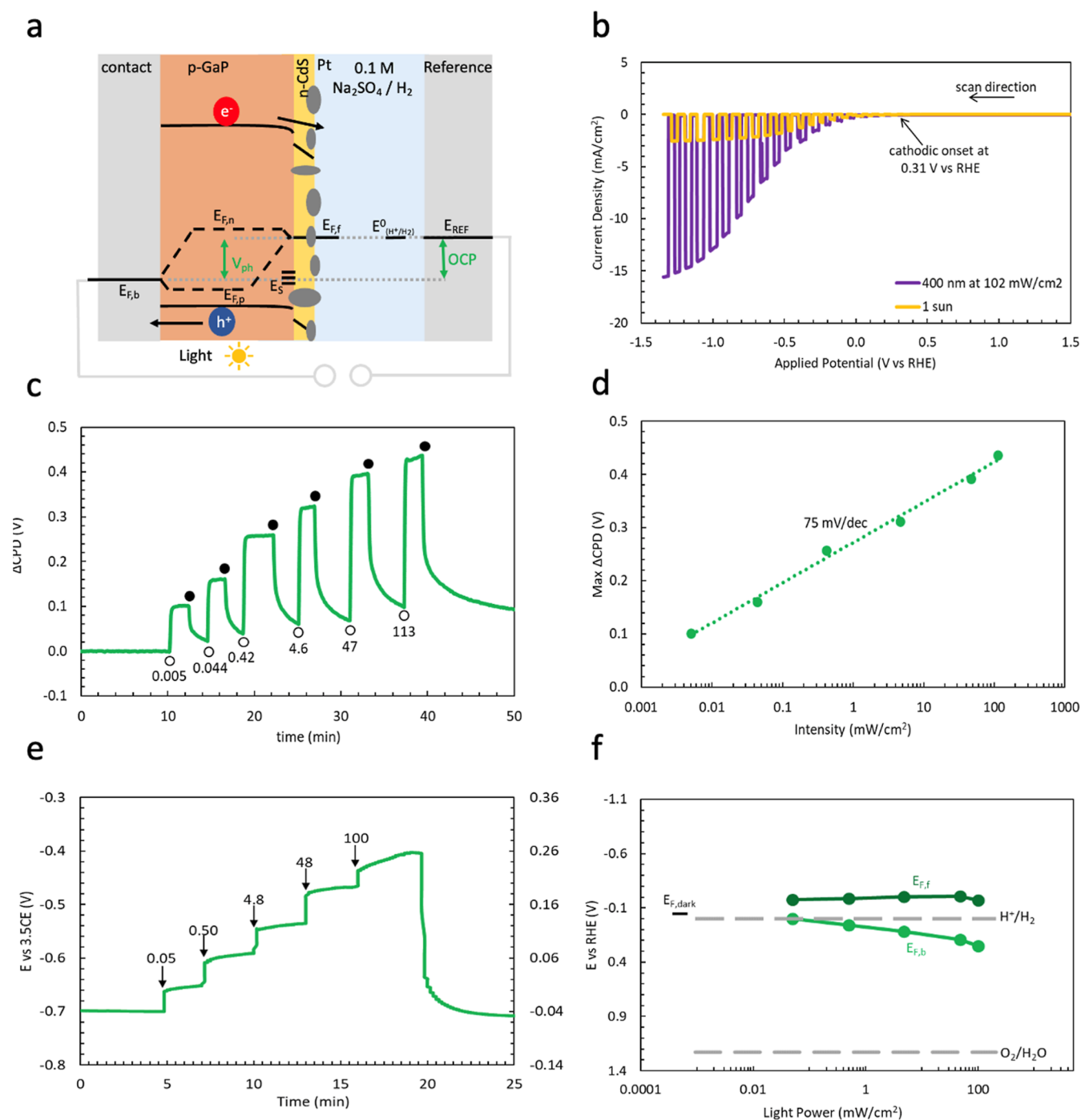
Figure 8. GaP/CdS/Pt in aqueous Na_2SO_4 at pH 6.9 under 10% H_2 in N_2 flow. (a) Qualitative junction scheme under illumination. (b) Linear sweep voltammetry scans under chopped illumination. (c) Intensity dependent SPV from a 405 nm LED (irradiance in units of mW/cm^2) and (d) maximum ΔCPD versus logarithm of light intensity. (e) Intensity dependent OCP under 400 nm LED illumination displayed in units of mW/cm^2 versus calomel electrode (left) and RHE (right) (f) Fermi level diagram with $E_{F,b}$ from OCP data and $E_{F,f}$ from SPV data and eq 1.

photovoltage from OCP (0.13 V at 100 mW cm^{-2}) is also much smaller than seen in 0.1 H_2SO_4 solution (N_2). These observations point toward a less effective solid−liquid junction in neutral Na_2SO_4 solution. This degraded junction is caused by a lower built-in potential, as seen from the more oxidizing E_F value in the dark (0.61 V RHE in neutral electrolyte, versus 0.22−0.28 V RHE in acidic solution). We hypothesize, that this is a result of the slower charge transfer kinetics between the electrode and the electrolyte. Because no fast redox couples (H_2/H_2O, or O_2/H_2O) are present, the E_F value of the electrode

is controlled by the combined work functions of Pt (5.64 eV, +1.20 V vs RHE for polycrystalline Pt)[55] and CdS (−0.1 V RHE).

To probe the effect of added O_2, measurements were repeated in 0.1 M Na_2SO_4 saturated with O_2 at 1.0 atm. This time (Figure 7), the cathodic photocurrent reaches only 0.26 mA cm^{-2} at 0 V vs RHE, which is 15% of the photocurrent in 0.1 M Na_2SO_4 (N_2). The photocurrent onset is at 0.62 V vs RHE, but the photovoltage cannot be extracted from the PEC data because it is not clear if protons or oxygen are being reduced. Lastly,
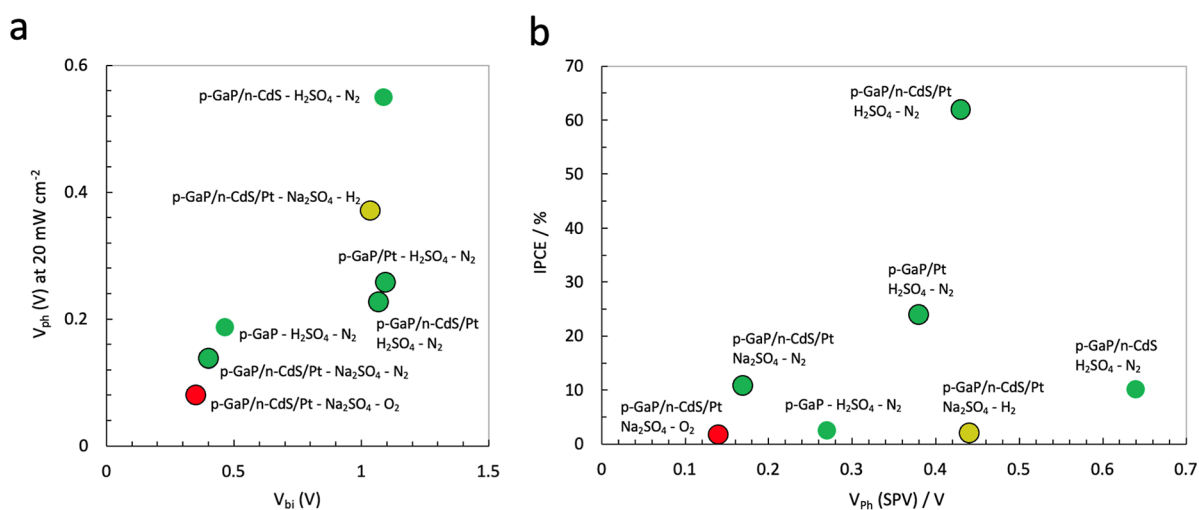
Figure 9. Plot of the (a) open circuit photovoltage V_{Ph}(SPV) at 405 nm (20 mW cm^{-2}) versus the built-in potential $V_{Bi} = E_{FB} - E_F$ (dark). (b) IPCE versus V_{Ph}(SPV) at 405 nm (20 mW cm^{-2}). Green: N$_2$ gas, yellow: H$_2$ gas, red: O$_2$ gas, black boundary: Pt. All values from Table 1.

sawtoothed shaped photocurrent transients appear, that are a sign of trapping and detrapping of electrons at the photo-electrode surface.[35] This may involve the chemisorbed O$_2$/O$_2^-$ (superoxide) redox couple. Transient LED illumination (Figure 7c) produces positive SPV signals, but the values are small (0.12 V) and near zero under the weakest illumination (0.003 mW cm^{-2}). Based on the change of the E_F under 100 mW cm^{-2} illumination, a V_{Ph}(OCP) of up to 0.18 V develops, as shown in Figure 7e. This is much smaller than seen in 0.1 M H$_2$SO$_4$ (N$_2$) solution (0.26 at 75 mW cm^{-2}). In the dark, a Fermi level of 0.70 V vs RHE was recorded, which increases to 0.72 V after the illumination cycle is finished. These positive values are likely due to adsorbed O$_2$ and the associated O$_2$/H$_2$O$_2$ reduction potential of 0.70 V RHE.[56]

Looking at the Fermi energy diagram in Figure 7f, it can be seen that the minority carrier potential at the front of the electrode $E_{F,f}$ is pinned to the O$_2$/H$_2$O$_2$ reduction potential (0.70 V) RHE throughout the experiment. This occurs because in the presence of 1.0 atm O$_2$ and 10^{-7} M H$_3$O$^+$, O$_2$ reduction is approximately 10^7 times much faster than proton reduction. This reduces the built-in potential of the junction and its photovoltage output. Based on the 0.62 V vs RHE photocurrent onset in Figure 7b the energy conversion efficiency of this O$_2$ reduction photocathode is zero.

Lastly, PEC data for the GaP/CdS/Pt electrode in 0.1 M Na$_2$SO$_4$ saturated with forming gas (10% H$_2$ and 90% N$_2$) are shown in Figure 8. The cathodic photocurrent is found to be 1.7 mA cm^{-2} at 0 V vs RHE (IPCE = 1.96%) and the photovoltage, V_{Ph}(PEC) is 0.31 V. The SPV reaches 0.44 V (Figure 8c), which is 2.5 and 4 times the value in N$_2$ or O$_2$ atmosphere, respectively. Illumination is accompanied by the formation of small gas bubbles on the surface of the electrode (Figure S11), indicating successful proton reduction to H$_2$, without any applied bias. Based on the positive CPD baseline drift in Figure 8c this charge transfer is irreversible. It is caused by the the diffusion of hydrogen gas away from the electrode.

Based on the SPV vs Log I data in Figure 8d (slope 75 mV dec^{-1}), the junction is near ideal and generates photovoltage even at the lowest light intensity (0.05 mW cm^{-2}). The ability of the GaP/CdS/Pt electrode to generate H$_2$ without applied bias is reflected in the Fermi level diagram in Figure 8f. It shows an $E_{F,f}$ at −0.2 V vs RHE at all light intensities, sufficient for proton

reduction. In the dark, the E_F of −0.04 V RHE is also controlled by the electrochemical potential (0.0 V RHE) of the H$^+$/H$_2$ couple. This shows how fast charge transfer with the H$^+$/H$_2$ couple generates a strong built-in potential for charge separation.

The results in Figures 2−8 illustrate how the photovoltage and photocurrent of the GaP photocathode vary with the addition of Pt electrocatalysts and the CdS layer and depend also on the charge transfer kinetics of the redox couples in the electrolyte and their redox potentials. To better depict the influence of these parameters, a plot of the photovoltage versus the built-in potential V_{Bi} is shown in Figure 9a. A nearly linear relationship between V_{Ph} (the maximum free energy output of the electrode per electron) and V_{Bi} is seen for all GaP/CdS/Pt electrodes in Na$_2$SO$_4$ electrolyte. This is because the GaP/CdS/Pt liquid junctions are chemically identical and only differ in the redox properties of the gases, N$_2$, H$_2$/N$_2$(1:9), O$_2$ during the measurements. The linear correlation between V_{Bi} and V_{Ph} shows that the barrier height of the junction controls charge separation under illumination. However, photovoltages reach only ∼33% of the built-in potentials, which is attributed to electron−hole recombination at the GaP-Pt interface. Indeed, increased recombination at semiconductor-Pt contacts has been reported for n-GaInP$_2$/Pt photoelectrodes[57] and CdS/Pt photocatalysts.[58] In the absence of H$_2$, the GaP/Pt contact is entirely ohmic (due to the similarity of work functions), allowing charge carriers to recombine at the GaP/Pt interface.[59]

The effects of O$_2$ and H$_2$ on the charge separation efficiency of the junction are noteworthy in the context of water splitting photocatalysts because they predict improved activity in the presence of hydrogen (improves the semiconductor-liquid junction) and diminished activity in the presence of oxygen. The problem of O$_2$ as a competitive electron acceptor is already well-known. Suppressing this back reaction requires selective electrocatalysts, such as Rh/Cr$_2$O$_3$ or Rh$_{2-y}$Cr$_y$O$_3$.[53,60] The new results here show that O$_2$ is not just a competitive electron acceptor, but it is also degrading the p-type semiconductor-liquid junction by reducing the potential barrier V_{Bi}. This suggests that improved water splitting photocatalysts might be possible by preventing *electric* contact between O$_2$ and the proton reduction site.

To better understand the variables affecting the photocurrent of the various devices, IPCE values are plotted in Figure 9b versus the measured photovoltage. As expected, there is a correlation between the open circuit photovoltage and the photocurrent, but the correlation is weak and there are many exceptions. The highest IPCE values occur for electrodes containing a Pt cocatalyst, illustrating the importance of fast charge transfer kinetics (small overpotential) on electrode performance. For the GaP/CdS device the photocurrent is low because cadmium chalcogenides have significant proton reduction overpotentials.[47] This counters the positive effect of the p-/n-junction on the photovoltage. Similarly, the low IPCE of the GaP-H_2SO_4 electrode is a combination of the absence of the Pt cocatalyst and the presence of surface states which cause a low built-in voltage. Depressed IPCE values also result from the exchange of the H_2SO_4 electrolyte for Na_2SO_4. As the proton concentration in the latter is 10^7 lower, the proton reduction kinetics in Na_2SO_4 are much slower.[61] Interestingly, the presence of H_2 in the GaP/CdS/Pt−Na_2SO_4−H_2 system also reduces IPCE values. This is attributed to an increased H_2 diffusion overpotential.[61] Overall, Figure 9 shows that the charge separating ability (photovoltage) of GaP solar fuel electrodes is mainly controlled by the thermodynamics at the semiconductor interface (the built-in potential), as determined by the gradient of the electrochemical potential. The photocurrent on the other hand is mainly controlled by the charge transfer kinetics, as determined by the concentrations of the electron acceptors and by the electrocatalytic properties of the interface. Superior energy conversion performance, as in the GaP/CdS/Pt/H_2SO_4−N_2 device, is possible when neither charge transfer kinetics nor the built-in potential of the junction are limiting.

CONCLUSION

In summary, we evaluate the factors that control the photocurrent and open circuit photovoltage of GaP photoelectrodes for hydrogen evolution from water. The open circuit photovoltage of the bare GaP-liquid junction is limited by recombination at surface states. A CdS overlayer increases the GaP photovoltage and photocurrent due to formation of a n-p-junction. The junction also promotes carrier separation from surface states, but it does not remove the states, which remain visible in SPV spectra. An electrodeposited Pt cocatalyst increases the photocurrent due to improved HER kinetics, but reduces the photovoltage by causing charge recombination at the GaP/Pt interface. Added O_2 gas reduces the photovoltage by diminishing the electrostatic barrier (band bending) in the junction while added H_2 gas has the opposite effects. This characterizes the GaP/CdS/Pt electrode as a Schottky type junction, despite the CdS overlayer. This effect of the electrolyte on the junction is a result of electric contact between Pt and the GaP. Added H_2 or increased solution pH also reduce the photocurrent, due to the slower electron transfer kinetics. The higher performance (IPCE of 62% at 400 nm and photovoltage of 0.43 V at 250 mW cm^{-2}) of the GaP/CdS/Pt/H_2O champion device results from a balance between efficient charge separation and fast kinetics. This shows that both thermodynamics and kinetics are important to the operation of photoelectrodes and photocatalysts under low or zero applied bias. Additionally, the work shows that PEC or OCP data tends to underestimate the photovoltage because they do not account for changes in the electrochemical potential $E_{F,f}$ at the electrode-liquid contact, in Figures 3f, 4f and 5f, for example. The VKP-SPV method avoids

this problem by giving the open circuit photovoltage values directly as the SPV signal.

EXPERIMENTAL SECTION

Concentrated sulfuric acid (Sigma-Aldrich), hydrogen peroxide (30%, Fisher), thiourea (99%, Alfa Aesar), cadmium acetate dihydrate (analytical reagent, Mallinckrodt), ammonium hydroxide (29.7%, certified ACS plus, Fisher), hexachloroplatinic acid (99.9%, Alfa Aesar), and sodium sulfate (>99.0%, Sigma-Aldrich) were used as received. Water was purified using a Nanopure system to >16 MΩ cm resistivity. The p-type GaP wafer doped with zinc (polished/unpolished, carrier density of 6.8×10^{17} cm^{-3}) was obtained from *El-Cat* and manufactured by the Institute of Electronic Materials Technology. It was etched in a small beaker containing 3 mL sulfuric acid, 1 mL hydrogen peroxide, and 1 mL nanopure water (piranha acid) at 50 °C for 10 min. The wafer was washed 5 times with nanopure water to remove excess etchant and dried in the dark under a N_2 flow. All measurements were conducted on the nonpolished side of the wafer.

CdS Deposition. Thin CdS layers were fabricated using a modified procedure by Zhang and co-workers.[62] A freshly etched piece of GaP wafer was presoaked in 20 mL of an aqueous solution containing 7.5 mM cadmium acetate dihydrate and 2.5 M ammonium hydroxide at 80 °C for 10 min. Then the wafer was moved to a solution of 7.5 mM cadmium acetate dihydrate, 0.375 M thiourea, and 2.5 M ammonium hydroxide at 70 °C for an additional 10 min. The wafer was rinsed with water to remove excess reagents and allowed to dry for 15 min in air. Finally, the wafer was annealed in air at 300 °C for 1 h.

Pt Photodeposition. Following the procedure by Mali and co-workers,[63] an aqueous 50 mL solution of 0.1 M sodium sulfate and 10 μM hexachloroplatinic acid was prepared and placed into a 3-electrode electrochemical cell, using a Pt counter electrode and a 3.5 M SCE reference electrode. The GaP/CdS wafer was masked with polyethylene tape on the back side and lowered into the solution. The solution was then degassed with N_2 for 20 min before simulated 1 sun illumination and a bias of −0.75 V vs 3.5CE was applied for 1 h. The wafer was removed from the solution and rinsed with water and stored in the dark in air.

SPV measurements were conducted using a circular (2.5 mm diameter), semitransparent vibrating gold mesh disk (*Kelvin Probe S*) that was mounted inside of a home-built vacuum chamber and controlled by a Kelvin Control 7 Oscillator/amplifier (all from *Besocke Delta Phi*). Samples were grounded electrically via an allegator clip and 10 μL of electrolyte was pipetted onto the electrode and a microscopy cover glass (*Fisher Scientific*, 0.17 to 0.25 mm thickness) was placed over the liquid. The Kelvin probe was lowered 1−2 mm above the sample. The spectrum was measured with light from a 300 W xenon lamp filtered through an Oriel Cornerstone 130 monochromator in the 0.4−5.0 eV interval. During the measurements, the chamber was purged continuously (1 L/min) with N_2 or O_2 or H_2/N_2 gas saturated with water to prevent drying of electrolyte. Intensity dependent SPV measurements were conducted with an air-cooled 405 nm LED in the 0.004 and 250 mW/cm^2 intensity range. The baseline was corrected by subtracting a fit of a dark scan.

PEC measurements were conducted in a three-electrode setup with a Pt counter electrode and a 3.5 M calomel reference electrode (3.5CE). The GaP working electrode had the back side covered with polyestertape and was connected using a

copper clip. The exposed area was measured graphically (imageJ) to calculate current density. The solution and enclosed head space was purged with N_2 gas to remove oxygen for >15 min or until the measured OCP had no more drift. The working electrode was calibrated using the potential (E^0 = +0.358 V vs NHE) of the $K_{4/3}[Fe(CN)_6]/Fe(CN)_6^{4-}$ redox couple. A 300 W Xe lamp equipped with an infrared filter was used as the light source and the distance was adjusted to have an intensity of 100 mW/cm^2 (1 sun) at the working electrode. The irradiance was measured with using a photometer equipped with a GaAsP light detector (International Light Technologies, Inc.). OCP measurements were performed using light from an air cooled 400 nm LED with an irradiance between 0.003 and 100 mW/cm^2. The voltage was regulated with a DC power supply and its intensity measured by a photometer equipped with a GaAsP UV−vis detector (International Light Technologies, Inc.). Several light on/off cycles were used to determine the electrode potential in the dark once it stabilized. UV−vis diffuse reflectance spectra were recorded on the wafer using a Thermo Scientific Evolution 220 spectrometer after calibration with a $BaSO_4$ disc as a reference. SEM and EDX were performed on a Scios DualBeam SEM/FIB instrument with an accelerating voltage of 10−20 kV.

■ ASSOCIATED CONTENT

Ⓢ Supporting Information

The Supporting Information is available free of charge at https://pubs.acs.org/doi/10.1021/acs.jpcc.4c04955.

> PEC scans, photos, diffuse reflectance and emission optical spectra, photovoltage data, energy diagrams, scanning electron micrographs and element dispersive spectroscopy data (PDF)

■ AUTHOR INFORMATION

Corresponding Author

Frank E. Osterloh − *Department of Chemistry, University of California, Davis, California 95616, United States;* ⓞ orcid.org/0000-0002-9288-3407; Email: fosterloh@ucdavis.edu

Authors

Kathleen Becker − *Department of Chemistry, University of California, Davis, California 95616, United States*

Li Wang − *Department of Chemistry, University of California, Davis, California 95616, United States*

Complete contact information is available at:
https://pubs.acs.org/10.1021/acs.jpcc.4c04955

Notes

The authors declare no competing financial interest.

■ ACKNOWLEDGMENTS

■ REFERENCES

(1) Fabian, D. M.; Hu, S.; Singh, N.; Houle, F. A.; Hisatomi, T.; Domen, K.; Osterloh, F. E.; Ardo, S. Particle Suspension Reactors and Materials for Solar-Driven Water Splitting. *Energy Environ. Sci.* **2015**, *8*, 2825−2850.

(2) Kudo, A.; Miseki, Y. Heterogeneous Photocatalyst Materials for Water Splitting. *Chem. Soc. Rev.* **2009**, *38*, 253−278.

(3) Walter, M. G.; Warren, E. L.; McKone, J. R.; Boettcher, S. W.; Mi, Q. X.; Santori, E. A.; Lewis, N. S. Solar Water Splitting Cells. *Chem. Rev.* **2010**, *110*, 6446−6473.

(4) Jia, J.; Seitz, L. C.; Benck, J. D.; Huo, Y.; Chen, Y.; Ng, J. W. D.; Bilir, T.; Harris, J. S.; Jaramillo, T. F. Solar Water Splitting by Photovoltaic-Electrolysis with a Solar-to-Hydrogen Efficiency Over 30%. *Nat. Commun.* **2016**, *7*, 13237.

(5) Fehr, A. M. K.; Agrawal, A.; Mandani, F.; Conrad, C. L.; Jiang, Q.; Park, S. Y.; Alley, O.; Li, B.; Sidhik, S.; Metcalf, I.; et al. Integrated Halide Perovskite Photoelectrochemical Cells with Solar-Driven Water-Splitting Efficiency of 20.8%. *Nat. Commun.* **2023**, *14*, 3797.

(6) Wang, Q.; Hisatomi, T.; Suzuki, Y.; Pan, Z.; Seo, J.; Katayama, M.; Minegishi, T.; Nishiyama, H.; Takata, T.; Seki, K.; et al. Particulate Photocatalyst Sheets Based on Carbon Conductor Layer for Efficient Z-Scheme Pure-Water Splitting at Ambient Pressure. *J. Am. Chem. Soc.* **2017**, *139*, 1675−1683.

(7) Takata, T.; Jiang, J.; Sakata, Y.; Nakabayashi, M.; Shibata, N.; Nandal, V.; Seki, K.; Hisatomi, T.; Domen, K. Photocatalytic Water Splitting with a Quantum Efficiency of Almost Unity. *Nature* **2020**, *581*, 411−414.

(8) Chen, S.; Wang, L.-W. Thermodynamic Oxidation and Reduction Potentials of Photocatalytic Semiconductors in Aqueous Solution. *Chem. Mater.* **2012**, *24*, 3659−3666.

(9) Sivula, K.; van de Krol, R. Semiconducting Materials for Photoelectrochemical Energy Conversion. *Nat. Rev. Mater.* **2016**, *1*, 15010.

(10) Zhou, P.; Navid, I. A.; Ma, Y.; Xiao, Y.; Wang, P.; Ye, Z.; Zhou, B.; Sun, K.; Mi, Z. Solar-to-Hydrogen Efficiency of More than 9% in Photocatalytic Water Splitting. *Nature* **2023**, *613*, 66−70.

(11) Kuang, Y.; Jia, Q.; Ma, G.; Hisatomi, T.; Minegishi, T.; Nishiyama, H.; Nakabayashi, M.; Shibata, N.; Yamada, T.; Kudo, A.; et al. Ultrastable Low-Bias Water Splitting Photoanodes Via Photo-corrosion Inhibition and In Situ Catalyst Regeneration. *Nat. Energy* **2017**, *2*, 16191.

(12) Shi, X.; Choi, I. Y.; Zhang, K.; Kwon, J.; Kim, D. Y.; Lee, J. K.; Oh, S. H.; Kim, J. K.; Park, J. H. Efficient Photoelectrochemical Hydrogen Production from Bismuth Vanadate-Decorated Tungsten Trioxide Helix Nanostructures. *Nat. Commun.* **2014**, *5*, 4775.

(13) Pihosh, Y.; Turkevych, I.; Mawatari, K.; Uemura, J.; Kazoe, Y.; Kosar, S.; Makita, K.; Sugaya, T.; Matsui, T.; Fujita, D.; et al. Photocatalytic Generation of Hydrogen by Core-Shell $WO_3/BiVO_4$ Nanorods with Ultimate Water Splitting Efficiency. *Sci. Rep.* **2015**, *5*, 11141.

(14) Goto, Y.; Hisatomi, T.; Wang, Q.; Higashi, T.; Ishikiriyama, K.; Maeda, T.; Sakata, Y.; Okunaka, S.; Tokudome, H.; Katayama, M.; et al. A Particulate Photocatalyst Water-Splitting Panel for Large-Scale Solar Hydrogen Generation. *Joule* **2018**, *2*, 509−520.

(15) Lyu, H.; Hisatomi, T.; Goto, Y.; Yoshida, M.; Higashi, T.; Katayama, M.; Takata, T.; Minegishi, T.; Nishiyama, H.; Yamada, T.; et al. An Al-Doped $SrTiO_3$ Photocatalyst Maintaining Sunlight-Driven Overall Water Splitting Activity for over 1000 h of Constant Illumination. *Chem. Sci.* **2019**, *10*, 3196−3201.

(16) Madelung, O. *Semiconductors: Data Handbook*, 3rd ed.; Springer: Berlin, 2004; p 691.

(17) Becker, K.; Xiao, C.; Assavachin, S.; Kundmann, A.; Osterloh, F. E. 14.8% Quantum Efficient Gallium Phosphide Photocatalyst for Hydrogen Evolution. *J. Am. Chem. Soc.* **2024**, *146*, 7723−7733.

(18) Standing, A.; Assali, S.; Gao, L.; Verheijen, M. A.; van Dam, D.; Cui, Y.; Notten, P. H. L.; Haverkort, J. E. M.; Bakkers, E. P. A. M. Efficient Water Reduction with Gallium Phosphide Nanowires. *Nat. Commun.* **2015**, *6*, 7824.

(19) Nozik, A. J. P-N Photoelectrolysis Cells. *Appl. Phys. Lett.* **1976**, *29*, 150−153.

(20) Krawicz, A.; Cedeno, D.; Moore, G. F. Energetics and Efficiency Analysis of a Cobaloxime-Modified Semiconductor under Simulated Air Mass 1.5 Illumination. *Phys. Chem. Chem. Phys.* **2014**, *16*, 15818−15824.

(21) Malizia, M.; Seger, B.; Chorkendorff, I.; Vesborg, P. C. K. Formation of a P–N Heterojunction on GaP Photocathodes for H2 Production Providing an Open-Circuit Voltage of 710 Mv. *J. Mater. Chem. A* **2014**, *2*, 6847–6853.

(22) Lee, S.; Bielinski, A. R.; Fahrenkrug, E.; Dasgupta, N. P.; Maldonado, S. Macroporous P-Gap Photocathodes Prepared by Anodic Etching and Atomic Layer Deposition Doping. *ACS Appl. Mater. Interfaces* **2016**, *8*, 16178–16185.

(23) Hu, S.; Shaner, M. R.; Beardslee, J. A.; Lichterman, M.; Brunschwig, B. S.; Lewis, N. S. Amorphous TiO_2 Coatings Stabilize Si, GaAs, and GaP Photoanodes for Efficient Water Oxidation. *Science* **2014**, *344*, 1005–1009.

(24) Xu, Z.; Hou, B.; Zhao, F.; Suo, S.; Liu, Y.; Shi, H.; Cai, Z.; Hill, C. L.; Musaev, D. G.; Mecklenburg, M.; et al. Direct In Situ Measurement of Quantum Efficiencies of Charge Separation and Proton Reduction at TiO_2-Protected GaP Photocathodes. *J. Am. Chem. Soc.* **2023**, *145*, 2860–2869.

(25) Brown, E. S.; Peczonczyk, S. L.; Wang, Z.; Maldonado, S. Photoelectrochemical Properties of CH3-Terminated P-Type GaP(111)A. *J. Phys. Chem. C* **2014**, *118*, 11593–11600.

(26) Sze, S. M. *Semiconductor Devices, Physics and Technology*, 2nd ed.; Wiley: New York, 2002; p 564.

(27) Hamann, T. W.; Gstrein, F.; Brunschwig, B. S.; Lewis, N. S. Measurement of the Free-Energy Dependence of Interfacial Charge-Transfer Rate Constants Using ZnO/H_2O Semiconductor/Liquid Contacts. *J. Am. Chem. Soc.* **2005**, *127*, 7815–7824.

(28) Aspnes, D. E.; Heller, A. Photoelectrochemical Hydrogen Evolution and Water Photolyzing Semiconductor Suspensions: Properties of Platinum Group Metal Catalyst-Semiconductor Contacts in Air and in Hydrogen. *J. Phys. Chem. C* **1983**, *87*, 4919–4929.

(29) Hemmerling, J. R.; Mathur, A.; Linic, S. Design Principles for Efficient and Stable Water Splitting Photoelectrocatalysts. *Acc. Chem. Res.* **2021**, *54*, 1992–2002.

(30) Pan, Z.; Yanagi, R.; Wang, Q.; Shen, X.; Zhu, Q.; Xue, Y.; Röhr, J. A.; Hisatomi, T.; Domen, K.; Hu, S. Mutually-Dependent Kinetics and Energetics of Photocatalyst/Co-Catalyst/Two-Redox Liquid Junctions. *Energy Environ. Sci.* **2020**, *13*, 162–173.

(31) Cheng, Y.; Xiao, C.; Mahmoudi, B.; Scheer, R.; Maijenburg, A. W.; Osterloh, F. E. Effect of Charge Selective Contacts on the Quasi Fermi Level Splitting of $CuGa_3Se_5$ Thin Film Photocathodes for Hydrogen Evolution and Methylviologen Reduction. *EES Catal.* **2023**, *1*, 74–83.

(32) Daemi, S.; Kundmann, A.; Becker, K.; Cendula, P.; Osterloh, F. E. Contactless Measurement of the Photovoltage in $BiVO_4$ Photoelectrodes. *Energy Environ. Sci.* **2023**, *16*, 4530–4538.

(33) Laskowski, F. A. L.; Oener, S. Z.; Nellist, M. R.; Gordon, A. M.; Bain, D. C.; Fehrs, J. L.; Boettcher, S. W. Nanoscale Semiconductor/ Catalyst Interfaces in Photoelectrochemistry. *Nat. Mater.* **2020**, *19*, 69–76.

(34) Pan, Z.; Röhr, J. A.; Ye, Z.; Fishman, Z. S.; Zhu, Q.; Shen, X.; Hu, S. Elucidating Charge Separation in Particulate Photocatalysts Using Nearly Intrinsic Semiconductors with Small Asymmetric Band Bending. *Sustain. Energy Fuels* **2019**, *3*, 850–864.

(35) Nellist, M. R.; Laskowski, F. A. L.; Lin, F.; Mills, T. J.; Boettcher, S. W. Semiconductor–Electrocatalyst Interfaces: Theory, Experiment, and Applications in Photoelectrochemical Water Splitting. *Acc. Chem. Res.* **2016**, *49*, 733–740.

(36) Bard, A. J.; Bocarsly, A. B.; Fan, F. R. F.; Walton, E. G.; Wrighton, M. S. The Concept of Fermi Level Pinning at Semiconductor-Liquid Junctions—Consequences for Energy-Conversion Efficiency and Selection of Useful Solution Redox Couples in Solar Devices. *J. Am. Chem. Soc.* **1980**, *102*, 3671–3677.

(37) Han, R.; Melo, M. A., Jr.; Zhao, Z.; Wu, Z.; Osterloh, F. E. Light Intensity Dependence of Photochemical Charge Separation in the $BiVO_4$/Ru-$SrTiO_3$:Rh Direct Contact Tandem Photocatalyst for Overall Water Splitting. *J. Phys. Chem. C* **2020**, *124*, 9724–9733.

(38) Liu, Y.; Guijarro, N.; Sivula, K. Understanding Surface Recombination Processes Using Intensity-Modulated Photovoltage Spectroscopy on Hematite Photoanodes for Solar Water Splitting. *Helv. Chim. Acta* **2020**, *103*, No. e2000064.

(39) Kumar, A.; Santangelo, P. G.; Lewis, N. S. Electrolysis of Water at Strontium Titanate ($SrTiO_3$) Photoelectrodes: Distinguishing between the Statistical and Stochastic Formalisms for Electron-Transfer Processes in Fuel-Forming Photoelectrochemical Systems. *J. Phys. Chem.* **1992**, *96*, 834–842.

(40) Daemi, S.; Kaushik, S.; Das, S.; Hamann, T. W.; Osterloh, F. E. $BiVO_4$–Liquid Junction Photovoltaic Cell with 0.2% Solar Energy Conversion Efficiency. *J. Am. Chem. Soc.* **2023**, *145*, 25797–25805.

(41) Nellist, M. R.; Laskowski, F. A. L.; Qiu, J.; Hajibabaei, H.; Sivula, K.; Hamann, T. W.; Boettcher, S. W. Potential-Sensing Electrochemical Atomic Force Microscopy for in Operando Analysis of Water-Splitting Catalysts and Interfaces. *Nat. Energy* **2018**, *3*, 46–52.

(42) Zhao, Z.; Willard, E. J.; Dominguez, J. R.; Wu, Z.; Osterloh, F. E. Depletion Layer Controls Photocatalytic Hydrogen Evolution with P-Type Gallium Phosphide Particles. *J. Mater. Chem. A* **2019**, *7*, 18020–18029.

(43) Wuille Bille, B. A.; Kundmann, A. C.; Osterloh, F. E.; Velázquez, J. M. $Ln_{10}S_{14}O$ (Ln = La, Pr, Nd, Sm) Oxysulfides: A Series of Direct N-Type Semiconductors. *Chem. Mater.* **2022**, *34*, 7553–7562.

(44) Han, R.; Kim, T.-Y.; Hamann, T. W.; Osterloh, F. E. Photochemical Charge Separation and Dye Self-Oxidation Control Performance of Fluorescein, Rose Bengal, and Triphenylamine Dye-Sensitized Solar Cells. *J. Phys. Chem. C* **2020**, *124*, 26174–26183.

(45) Chae, S. Y.; Park, S. J.; Han, S. G.; Jung, H.; Kim, C.-W.; Jeong, C.; Joo, O.-S.; Min, B. K.; Hwang, Y. J. Enhanced Photocurrents with ZnS Passivated Cu(In,Ga)(Se,S)$_2$ Photocathodes Synthesized Using a Nonvacuum Process for Solar Water Splitting. *J. Am. Chem. Soc.* **2016**, *138*, 15673–15681.

(46) Doughty, R. M.; Chowdhury, F. A.; Mi, Z.; Osterloh, F. E. Surface Photovoltage Spectroscopy Observes Junctions and Carrier Separation in Gallium Nitride Nanowire Arrays for Overall Water-Splitting. *J. Chem. Phys.* **2020**, *153*, 144707.

(47) Zhao, J.; Holmes, M. A.; Osterloh, F. E. Quantum Confinement Controls Photocatalysis—A Free Energy Analysis for Photocatalytic Proton Reduction at CdSe Nanocrystals. *ACS Nano* **2013**, *7*, 4316–4325.

(48) Pan, L.; Kim, J. H.; Mayer, M. T.; Son, M.-K.; Ummadisingu, A.; Lee, J. S.; Hagfeldt, A.; Luo, J.; Grätzel, M. Boosting the Performance of Cu_2O Photocathodes for Unassisted Solar Water Splitting Devices. *Nat. Catal.* **2018**, *1*, 412–420.

(49) Dai, P.; Li, W.; Xie, J.; He, Y.; Thorne, J.; McMahon, G.; Zhan, J.; Wang, D. Forming Buried Junctions to Enhance the Photovoltage Generated by Cuprous Oxide in Aqueous Solutions. *Angew. Chem., Int. Ed.* **2014**, *53*, 13493–13497.

(50) Gao, L.; Cui, Y.; Vervuurt, R. H. J.; van Dam, D.; van Veldhoven, R. P. J.; Hofmann, J. P.; Bol, A. A.; Haverkort, J. E. M.; Notten, P. H. L.; Bakkers, E. P. A. M.; et al. High-Efficiency InP-Based Photocathode for Hydrogen Production by Interface Energetics Design and Photon Management. *Adv. Funct. Mater.* **2016**, *26*, 679–686.

(51) Zhong, M.; Hisatomi, T.; Kuang, Y.; Zhao, J.; Liu, M.; Iwase, A.; Jia, Q.; Nishiyama, H.; Minegishi, T.; Nakabayashi, M.; et al. Surface Modification of CoO_x Loaded $BiVO_4$ Photoanodes with Ultrathin p-Type NiO Layers for Improved Solar Water Oxidation. *J. Am. Chem. Soc.* **2015**, *137*, 5053–5060.

(52) Vijselaar, W.; Kunturu, P. P.; Moehl, T.; Tilley, S. D.; Huskens, J. Tandem Cuprous Oxide/Silicon Microwire Hydrogen-Evolving Photocathode with Photovoltage Exceeding 1.3 V. *ACS Energy Lett.* **2019**, *4*, 2287–2294.

(53) Maeda, K.; Teramura, K.; Lu, D. L.; Takata, T.; Saito, N.; Inoue, Y.; Domen, K. Photocatalyst Releasing Hydrogen from Water. *Nature* **2006**, *440*, 295.

(54) Wang, Q.; Hisatomi, T.; Jia, Q.; Tokudome, H.; Zhong, M.; Wang, C.; Pan, Z.; Takata, T.; Nakabayashi, M.; Shibata, N.; et al. Scalable Water Splitting on Particulate Photocatalyst Sheets with a Solar-to-Hydrogen Energy Conversion Efficiency Exceeding 1%. *Nat. Mater.* **2016**, *15*, 611–615.

(55) Michaelson, H. B. Electron Work Function of the Elements. In *CRC Handbook of Chemistry and Physics*, 88 (Internet Version 2008) ed.; Lide, D. R., Ed.; CRC Press/Taylor and Francis: Boca Raton, FL, 2008.

(56) Vanysek, P. Electrochemical Series. In *CRC Handbook of Chemistry and Physics*, 88 (Internet Version 2008) ed.; CRC Press/Taylor and Francis: Boca Raton, FL, 2008.

(57) Yang, Y.; Gu, J.; Young, J. L.; Miller, E. M.; Turner, J. A.; Neale, N. R.; Beard, M. C. Semiconductor Interfacial Carrier Dynamics Via Photoinduced Electric Fields. *Science* **2015**, *350*, 1061−1065.

(58) Uchihara, T.; Matsumura, M.; Yamamoto, A.; Tsubomura, H. Effect of Platinum Loading on the Photocatalytic Activity and Luminescence of Cadmium-Sulfide Powder. *J. Phys. Chem.* **1989**, *93*, 5870−5874.

(59) Dittrich, T. *Materials Concepts for Solar Cells*; Imperial College Press: London, 2015; pp 197−516.

(60) Maeda, K.; Teramura, K.; Lu, D. L.; Saito, N.; Inoue, Y.; Domen, K. Noble-Metal/Cr_2O_3 Core/Shell Nanoparticles as a Cocatalyst for Photocatalytic Overall Water Splitting. *Angew. Chem., Int. Ed. Engl.* **2006**, *45*, 7806−7809.

(61) Sheng, W.; Gasteiger, H. A.; Shao-Horn, Y. Hydrogen Oxidation and Evolution Reaction Kinetics on Platinum: Acid Vs Alkaline Electrolytes. *J. Electrochem. Soc.* **2010**, *157*, B1529.

(62) Zhang, L.; Minegishi, T.; Nakabayashi, M.; Suzuki, Y.; Seki, K.; Shibata, N.; Kubota, J.; Domen, K. Durable Hydrogen Evolution from Water Driven by Sunlight Using (Ag,Cu)GaSe2 Photocathodes Modified with CdS and CuGa3Se5. *Chem. Sci.* **2015**, *6*, 894−901.

(63) Mali, M. G.; Yoon, H.; Joshi, B. N.; Park, H.; Al-Deyab, S. S.; Lim, D. C.; Ahn, S.; Nervi, C.; Yoon, S. S. Enhanced Photoelectrochemical Solar Water Splitting Using a Platinum-Decorated CIGS/CdS/ZnO Photocathode. *ACS Appl. Mater. Interfaces* **2015**, *7*, 21619−21625.